AIMS Energy, 14(2): 449–471.
DOI: 10.3934/energy.2026019
Received: 11 December 2025
Revised: 16 March 2026
Accepted: 16 April 2026
Published: 28 April 2026

http://www.aimspress.com/journal/energy

Research article

The coordinated ramp-frequency regulation optimization strategy considering energy storage capacity uncertainty

Haiyun An[1], Tianhui Zhao[1], Yuqing Bao[2,*] and Jingbo Zhao[1]

[1] Electric Power Research Institute, State Grid Jiangsu Electric Power Co., Ltd., 211103, China
[2] Nanjing Normal University, 210046, China

*** Correspondence:** Email: baoyuqing@njnu.edu.cn; Tel: +8615861813535.

Abstract: Energy storage systems (ESSs) serve as flexible resources that significantly contribute to the integration of uncertain renewable energy sources. They can mitigate power fluctuations through fast charging and discharging in ramping services while providing frequency regulation reserves to maintain system stability. However, traditional methods often neglect the uncertainty of storage capacity and the coupling between ramping and frequency regulation constraints, leading to potential capacity violations and inefficient joint optimization. In this paper, we propose a coordinated ramping-frequency regulation optimization strategy considering ESS capacity uncertainty. A probabilistic confidence-based model was developed to characterize the stochastic nature of capacity, and unified ramping-frequency regulation constraints were formulated for ESSs and thermal units. Nonlinear terms were linearized to derive a tractable mixed-integer quadratic programming (MIQP) model. Case studies verified that the proposed approach effectively accounts for capacity uncertainty, enables shared utilization of ramping and regulation capabilities under unified constraints, and enhances the overall efficiency of system flexibility deployment.

Keywords: energy storage systems; ramp; frequency regulation; capacity uncertainty; optimization

1. Introduction

With the large-scale integration of renewable energy sources (RESs) into power systems, their intermittency and uncertainty have posed significant challenges to secure and stable grid operation [1,2]. Taking wind and photovoltaic (PV) generation as examples, their outputs are strongly affected by

meteorological and seasonal variations, exhibiting pronounced volatility and randomness. In conventional power systems, thermal and hydropower units are mostly responsible for maintaining power balance, providing ramping capability, and performing frequency regulation. However, under high renewable penetration, their ramping and frequency regulation capacities are often insufficient to cope with the rapid variations in net load, which may lead to frequency deviations, aggravated power fluctuations, and reduced voltage stability [3,4].

Moreover, as a flexible resource, the energy storage system (ESS) has demonstrated great potential in mitigating renewable intermittency and enhancing system flexibility. With fast response and bidirectional charging-discharging capabilities, ESSs can participate in ramping services to absorb or supply power rapidly, thereby smoothing net load variations [5,6]. In addition, ESSs can provide frequency regulation and reserve capacity, contributing to system frequency support and reliability enhancement [7]. Through coordinated scheduling with conventional thermal units, ESSs can significantly improve overall system stability and operational efficiency.

Extensive research has been conducted on optimizing the scheduling strategies for ESSs participating in power system ramping and frequency regulation services.

The researchers in [8] examined a joint control strategy where energy storage coordinates with conventional generators for frequency regulation. Their method explicitly accounted for the ramping rate of generators alongside the energy management of the storage system to effectively mitigate load fluctuations. Moreover, the researchers in [9] presented a robust frequency-constrained unit commitment and multi-reserve resource allocation model for renewable-penetrated systems. By optimizing virtual inertia and droop factors to coordinate with synchronous generators, the proposed model stabilized system frequency and improved operational economics under uncertainty. The researchers in [10] explored a joint optimization framework using battery storage simultaneously for peak shaving and frequency regulation. Their results demonstrated a superlinear gain, indicating that jointly providing multiple services yields significantly larger economic benefits than utilizing the battery for individual applications. From the perspective of capacity allocation and demand-side management, the researchers in [11] explored a shared energy storage framework utilizing a game-theoretic approach. Their distributed optimization strategy for capacity trading and operation scheduling effectively minimized energy costs and reduced the peak-to-average ratio across the entire grid. The researchers in [12] proposed an uncertainty-aware mobile energy storage deployment strategy to enhance distribution system resilience. By considering the roles of ESSs in frequency regulation and power balancing, a robust optimization framework was developed that effectively reduced system risk and improved restoration capability. The researchers in [13] presented a two-stage hybrid optimization framework for aggregating distributed generalized storage systems, which jointly optimized ramping and regulation capacities to eliminate uncertainty impacts and significantly enhance utilization efficiency and system economy. The researchers in [14] investigated the co-optimization of battery storage for energy arbitrage and frequency regulation. To handle the large state space and multiple time scales, a multi-scale dynamic programming approach was introduced, enabling the ESS to make efficient scheduling decisions under stochastic conditions. The researchers in [15] proposed a chance-constrained scheduling model that incorporates primary frequency responses from aggregated electric vehicles. By using distributionally robust chance constraints to handle uncertainties in frequency regulation capacities and wind power forecasts, their method reduced system costs while enhancing reliability. The researchers in [16] proposed a battery energy storage model with charging-rate constraints for wind farm frequency regulation under uncertainty, jointly optimizing the cooperative

bidding of ESSs and thermal generators to improve robustness and reduce regulation costs. The researchers in [17] developed a multi-step assessment process using stochastic dynamic optimization and mixed-integer linear programming to determine the actual resource-adequacy contribution of energy storage providing frequency regulation, highlighting the significant impacts of state of energy (SOE) complexity and capacity limitations. To evaluate the economic viability of energy storage in power markets, The researchers in [18] developed operating schedules for battery energy storage companies providing peak shaving and spinning reserve services. By determining the optimum capacity of the energy storage systems, their approach maximized profits while contributing to grid frequency and voltage support under increasing wind penetration. The researchers in [19] proposed a frequency-constrained unit commitment model that integrates a coordinated frequency control strategy for wind turbines and energy storage systems. To overcome the computational challenges caused by strong nonlinear frequency nadir constraints, they introduced a multi-directional bilayer solution method, effectively reducing operating costs and ensuring system security. Addressing load and renewable uncertainties, the researchers in [20] presented a two-stage robust optimization framework for frequency stability-constrained microgrid scheduling. By deriving linearized restrictions for dynamic frequency metrics and leveraging the rapid response of energy storage, their model successfully mitigated transient power imbalances and maintained frequency deviations within safety thresholds. The researchers in [21] proposed a real-time cooperation scheme combining wind power and battery storage to jointly participate in energy and frequency regulation markets. By explicitly accounting for battery cycle life in their optimal bidding strategy, the method significantly increased overall revenue and improved regulation performance. At the system scheduling level, the researchers in [22] incorporated fast-response battery storage into a frequency dynamics-constrained unit commitment model to address wind generation uncertainty. To resolve computational challenges, they successfully applied a reformulation-linearization technique to transform the original nonlinear frequency constraints into a tractable mixed-integer linear programming problem, guaranteeing system security and economy.

Although significant progress has been made in the field, studies exhibit two major deficiencies concerning energy storage capacity uncertainty and ramp-frequency coordination:

1) Neglect of energy storage capacity uncertainty: Most optimization and control strategies for energy storage systems (ESS) assume a deterministic or fixed capacity. In practice, however, the available capacity of an ESS is influenced by factors such as battery degradation, temperature variations, and state of charge (SOC) estimation errors, leading to discrepancies between the actual and the expected available energy [23–25]. Failure to account for such uncertainties in capacity in the optimization model may result in capacity violation risks and deteriorated operational reliability.

2) Insufficient consideration of ramp-frequency coupling: In most studies, the ramping and frequency regulation services provided by thermal units and ESSs are modeled separately. Nevertheless, these two services typically share the same power output capacity in real-world operation. Ignoring this coupling may underestimate the benefits of joint resource allocation and lead to inefficient utilization of available flexibility resources.

To address the aforementioned issues, we propose a power system scheduling strategy that simultaneously considers energy storage capacity uncertainty and coordinated ramp-frequency optimization. A probabilistic confidence-based model is developed to characterize the uncertainty of energy storage capacity. On this basis, unified ramp-frequency constraints are formulated for the energy storage system (ESS) and thermal generating units. The nonlinear components of the model are

subsequently linearized to obtain a computationally tractable formulation. Finally, a coordinated optimization framework is established for the joint participation of ESS and thermal units in ramping and frequency regulation, which is solved using a mixed-integer quadratic programming (MIQP) approach.

The major contributions of this paper are summarized as follows:

1) A unified ramp-frequency regulation constraint model for ESS and thermal units is established. The reserve capacity requirements of both services are integrated into a unified framework, avoiding double-counting of shared physical capacity and more accurately capturing operational constraints.

2) A piecewise linearization model is developed for the nonlinear ramping characteristics of thermal units. The nonlinear problem is reformulated as a tractable MIQP model via piecewise linearization, achieving a balance between modeling accuracy and computational efficiency.

3) A chance-constrained model based on probabilistic confidence levels is formulated to address ESS capacity uncertainty. A chance-constrained programming approach transforms stochastic ESS capacity uncertainty into deterministic equivalent constraints at a prescribed confidence level, balancing system reliability and tractability.

The remainder of this paper is organized as follows: In Section 2, we develop the energy storage model considering capacity uncertainty. In Section 3, we formulate the linearized unified ramp-frequency constraint model for thermal units. In Section 4, we present the coordinated optimization scheduling model integrating ESS and thermal units. In Section 5, we provide the case studies and numerical analysis. Finally, in Section 6, we conclude the paper and discuss future work.

2. Energy storage model considering capacity uncertainty

In this section, we present the basic model of the ESS and then derive the energy constraint model considering capacity uncertainty.

2.1. Basic model of the energy storage system

The energy-power coupling constraint can be expressed as:

$$E_{e,t}^{*} = E_{e,t-1}^{*} + \eta_{ch} P_{e,t}^{ch} \Delta t - \frac{1}{\eta_{disch}} P_{e,t}^{disch} \Delta t \tag{1}$$

where $E_{e,t}$ denotes the stored energy of the ESS e at time t; $P_{e,t}^{ch}$ and $P_{e,t}^{disch}$ represent the charging and discharging power, respectively; η_{ch} and η_{disch} denote the charging and discharging efficiencies; and Δt is the time step. The ESS operation must also satisfy the following constraints:

$$\begin{cases} 0 \le P_{e,t}^{ch} \le P_{e}^{ch\max} \\ 0 \le P_{e,t}^{disch} \le P_{e}^{disch\max} \end{cases} \tag{2}$$

The electrical power output of the ESS, denoted as $P_{e,t}^{E}$, is expressed as:

$$P_{e,t}^{E} = P_{e,t}^{disch} - P_{e,t}^{ch} \tag{3}$$

The initial state of charge is required to be equal to the final state of charge, which can be expressed as:

$$E_{e,0}^{*} = E_{e,N_T}^{*} \tag{4}$$

which is a standard operational convention to ensure multi-period scheduling sustainability [21,22].

Since the ESS is simultaneously constrained by its maximum output power during ramping and frequency regulation, the unified ramp-frequency regulation constraint of the ESS can be expressed as:

$$\left|R_{e,t}^{E}\right| + r_{e,t}^{E} \le P_{e}^{disch\max} - P_{e,t}^{disch} \tag{5}$$

where $R_{e,t}^{E}$ and $r_{e,t}^{E}$ denote the power dispatched by the ESS for ramping and frequency regulation, respectively. Although ramping and frequency regulation involve minute-level and second-level physical responses, respectively, this unified constraint focuses on ex-ante capacity allocation at the scheduling stage. It mathematically constructs a static capacity envelope, ensuring that the pre-allocated capacities for both services share the same power headroom and never exceed the physical boundary of the ESS during real-time dynamic execution.

To linearize constraint Eq (5), auxiliary ramping variables $R_{e,t}^{E\uparrow}$ and $R_{e,t}^{E\downarrow}$ are introduced, which satisfy:

$$\begin{cases} R_{e,t}^{E} = R_{e,t}^{E\uparrow} - R_{e,t}^{E\downarrow} \\ R_{e,t}^{E\uparrow} \ge 0 \\ R_{e,t}^{E\downarrow} \ge 0 \end{cases} \tag{6}$$

Accordingly, the unified ramp-frequency regulation constraint Eq (5) for the ESS can be reformulated as:

$$R_{e,t}^{E\uparrow} + R_{e,t}^{E\downarrow} + r_{e,t}^{E} \le P_{e}^{disch\max} - P_{e,t}^{disch} \tag{7}$$

2.2. Energy storage capacity constraint model considering uncertainty

When capacity uncertainty is not considered, the energy (state-of-charge) constraints of the ESS can be expressed as:

$$E_{e}^{\min} \le E_{e,t} \le E_{e}^{\max} \tag{8}$$

where $E_{e}^{\max}$ and $E_{e}^{\min}$ denote the maximum and minimum allowable energy of the ESS, which are determined by the rated capacity and the SOC:

$$\begin{cases} E_{e}^{\max} = SoC_{e}^{U} \cdot E_{e}^{nom} \\ E_{e}^{\min} = SoC_{e}^{D} \cdot E_{e}^{nom} \end{cases} \tag{9}$$

where SoC_{e}^{U} and SoC_{e}^{D} are the upper and lower bounds of the SOC for unit e, and E_{e}^{nom} is the rated capacity of the storage system.

However, in practical operations, the exact amount of stored energy (i.e., the actual state of charge) in an ESS at any given time cannot be perfectly determined and is strictly subject to uncertainty. The

sources of this stored energy uncertainty primarily stem from:

1) The inherent measurement noise and precision errors of voltage and current sensors.

2) The dynamic variations in actual charge/discharge efficiencies caused by environmental temperature fluctuations and different power rates.

3) The gradual capacity degradation caused by continuous charge/discharge cycles and aging effects.

Given the complex and coupled nature of these factors, the overall uncertainty of the actual stored energy is commonly modeled as a normal distribution in engineering practice to ensure the mathematical tractability of the chance-constrained formulation.

When accounting for capacity uncertainty, the energy constraints of the ESS Eq (8) can be reformulated as a chance-constrained form:

$$\begin{cases} \Pr\{E_{e,t} \le E_e^{\max}\} \ge \eta_e \\ \Pr\{E_{e,t} \ge E_e^{\min}\} \ge \eta_e \end{cases} \tag{10}$$

where η_e represents the confidence level of the capacity constraint, which indicates that the probability of the stored energy of unit e at time t remaining within the allowable range is no less than η_e.

Assuming that the SOC of the ESS is uncertain, the actual stored energy $E_{e,t}$ follows a certain probability distribution. For instance, under a normal distribution, it can be expressed as:

$$E_{e,t} \sim E_{e,t}^{*} + N(0, \delta_{e,t}^2) \tag{11}$$

where $E_{e,t}^{*}$ denotes the nominal energy, i.e., the measured or estimated value of the actual stored energy $E_{e,t}$.

Based on the distribution function Eq (11), the chance constraint Eq (10) can be further converted as:

$$\begin{cases} \Phi\left\{\dfrac{E_e^{\max} - E_{e,t}^{*}}{\delta_{e,t}}\right\} \ge \eta_e \\ 1 - \Phi\left\{\dfrac{E_e^{\min} - E_{e,t}^{*}}{\delta_{e,t}}\right\} \ge \eta_e \end{cases} \tag{12}$$

where Φ is the cumulative distribution function of the normal distribution.

After simplification, the energy constraint can be expressed in the form given in Eq (13):

$$E_e^{\min} - \Phi^{-1}(1-\eta_e)\delta_{e,t} \le E_{e,t}^{*} \le E_e^{\max} - \Phi^{-1}(\eta_e)\delta_{e,t} \tag{13}$$

Due to the symmetry of the normal distribution, the following condition holds:

$$\Phi^{-1}(\eta_e) = -\Phi^{-1}(1-\eta_e) \tag{14}$$

Consequently, the energy constraint in Eq (13) can be further simplified as:

$$E_e^{\min} + \Phi^{-1}(\eta_e)\delta_{e,t} \le E_{e,t}^{*} \le E_e^{\max} - \Phi^{-1}(\eta_e)\delta_{e,t} \tag{15}$$

A schematic illustration of the energy constraint considering capacity uncertainty is shown in Figure 1. Compared with the deterministic constraint in Eq (8), constraint Eq (15) explicitly incorporates the confidence level of the ESS's capacity, effectively mitigating the risk of overcharging or overdischarging.

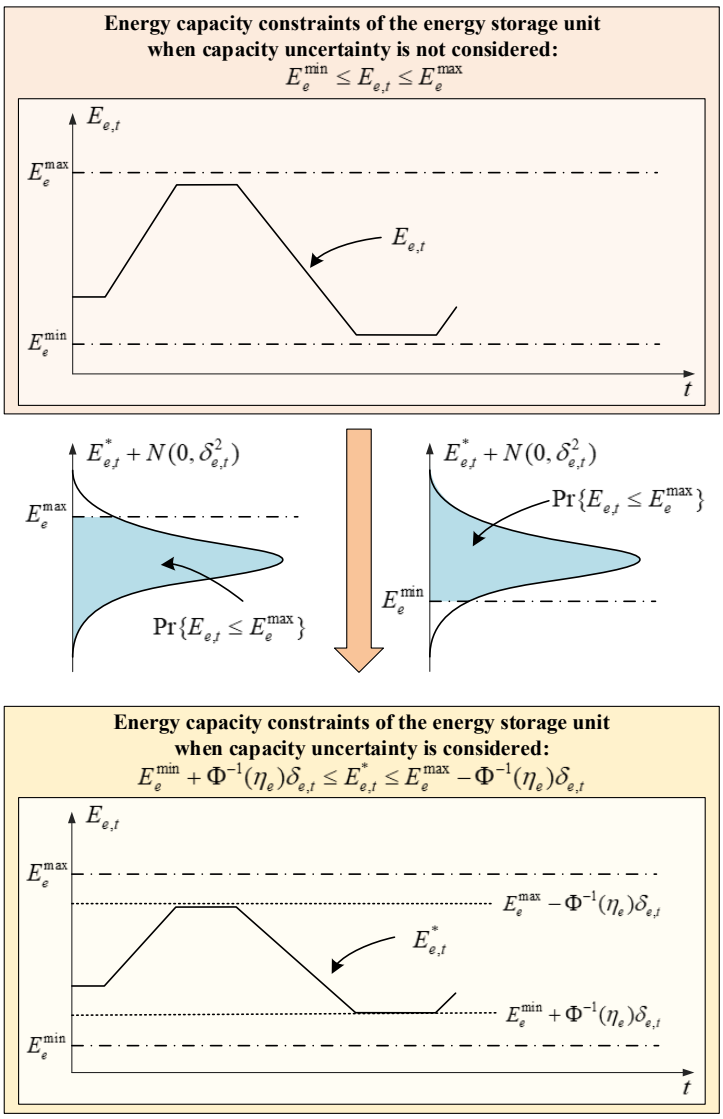

Figure 1. Energy capacity constraint under capacity uncertainty.

3. Thermal power unit model considering nonlinear regulation characteristics

3.1. Basic model of thermal power units

The upper and lower bounds of the output power of a thermal power unit can be expressed as:

$$u_{i,t} \cdot P_i^{G\min} \le P_{i,t}^G \le u_{i,t} \cdot P_i^{G\max} \tag{16}$$

where P_i^G denotes the output power of unit i, $P_i^{G\max}$ and $P_i^{G\min}$ represent the maximum and minimum generation limits of unit i, respectively, and $u_{i,t}$ is the on/off status of unit i at time t (1 indicates that the unit is online, and 0 indicates that it is offline).

The start-up and shut-down status $u_{i,t}$ of the thermal power unit must also satisfy the start-up/shut-down logic constraint:

$$\begin{cases} x_{i,t} - y_{i,t} = u_{i,t} - u_{i,t-1} \\ x_{i,t} + y_{i,t} \le 1 \end{cases} \tag{17}$$

where $x_{i,t}$ and $y_{i,t}$ represent the start-up and shut-down actions of unit i at time t, respectively.

The ramping of a thermal power unit is defined as the rate of change of its output power, which can be expressed as:

$$R_{i,t}^G = \frac{P_{i,t}^G - P_{i,t-1}^G}{\Delta t} \tag{18}$$

For units participating in ramping and frequency regulation, the output power is simultaneously constrained by the generation limits. The unified ramp-frequency regulation constraint can be formulated as:

$$\left| R_{i,t}^G \right| + r_{i,t}^G \le \min\left(P_i^{G\max} - P_{i,t}^G, R_{i,t}^{G\max} \right) \tag{19}$$

where $R_{i,t}^G$ and $r_{i,t}^G$ denote the portions of the output power of unit i at time t allocated to ramping and frequency regulation, respectively, and $R_{i,t}^{G\max}$ represents the ramping capability of unit i at time t.

Due to the mechanical inertia and the limitations of the fuel control system, the ramping capability of a thermal power unit typically exhibits a nonlinear relationship with its current output. The ramping capability $R_{i,t}^{G\max}$ can be approximated by a quadratic function, which can be expressed as:

$$R_{i,t}^{G\max} = \alpha_i^G + \beta_i^G \cdot P_{i,t}^G + \gamma_i^G \cdot \left(P_{i,t}^G \right)^2 \tag{20}$$

3.2. Linearized model of thermal power unit ramp-frequency regulation constraint

Since the thermal power unit model involves absolute value and min functions (constraint Eq (19)) as well as a quadratic function (constraint Eq (20)), linearization is required to facilitate the solution of the optimization problem.

First, the ramping variables $R_{i,t}^{G\uparrow}$ and $R_{i,t}^{G\downarrow}$ are defined, which satisfy:

$$\begin{cases} R_{i,t}^G = R_{i,t}^{G\uparrow} - R_{i,t}^{G\downarrow} \\ R_{i,t}^{G\uparrow} \ge 0 \\ R_{i,t}^{G\downarrow} \ge 0 \end{cases} \tag{21}$$

Accordingly, constraint Eq (19) can be linearized into two inequality constraints:

$$\begin{cases} R_{i,t}^{G\uparrow} + R_{i,t}^{G\downarrow} + r_{i,t}^{G} \le P_{i}^{G\max} - P_{i,t}^{G} \\ R_{i,t}^{G\uparrow} + R_{i,t}^{G\downarrow} + r_{i,t}^{G} \le R_{i,t}^{G\max} \end{cases} \tag{22}$$

Next, piecewise linearization (PWL) is performed to the ramping capability function in Eq (20). Assume that the output range of the thermal unit is divided into n_k segments. For each segment, the maximum and minimum power are denoted by $P_{i,k}^{GU}$ and $P_{i,k}^{GD}$, respectively, and the ramping capabilities at the segment endpoints are denoted by $R_{i,k}^{GU\max}$ and $R_{i,k}^{GD\max}$, with the slope of each segment denoted as $\varphi_{i,k}^{G}$. Using constraint Eq (19), the expressions for $R_{i,k}^{GU\max}$ and $R_{i,k}^{GD\max}$ can be obtained as:

$$\begin{cases} R_{i,k}^{GU\max} = \alpha_i^G + \beta_i^G \cdot P_{i,k}^{GU} + \gamma_i^G \cdot \left(P_{i,k}^{GU}\right)^2 \\ R_{i,k}^{GD\max} = \alpha_i^G + \beta_i^G \cdot P_{i,k}^{GD} + \gamma_i^G \cdot \left(P_{i,k}^{GD}\right)^2 \end{cases} \tag{23}$$

The slope $\varphi_{i,k}^{G}$ can be calculated as:

$$\varphi_{i,k}^{G} = \frac{R_{i,k}^{GU\max} - R_{i,k}^{GD\max}}{P_{i,k}^{GU} - P_{i,k}^{GD}} \tag{24}$$

On this basis, a binary variable $z_{i,k,t}^{G}$ is introduced to indicate whether thermal unit i is operating in segment k at time t, and a continuous variable $s_{i,k,t}^{G}$ represents the intra-segment offset. The variables $z_{i,k,t}^{G}$ and $s_{i,k,t}^{G}$ are further required to satisfy the following constraints:

$$\begin{cases} \sum_{k=1}^{n_k} z_{i,k,t}^{G} = u_{i,t} \\ 0 \le s_{i,k,t}^{G} \le z_{i,k,t}^{G} \cdot (P_{i,k}^{GU} - P_{i,k}^{GD}) \end{cases} \tag{25}$$

The relationship between the thermal unit power $P_{i,t}^{G}$ and the variables $z_{i,k,t}^{G}$ and $s_{i,k,t}^{G}$ can be expressed as:

$$P_{i,t}^{G} = \sum_{k=1}^{n_k} \left(P_{i,k}^{GD} \cdot z_{i,k,t}^{G} + s_{i,k,t}^{G} \right) \tag{26}$$

Based on this, a linearized expression for $R_{i,t}^{G\max}$ can be obtained using $z_{i,k,t}^{G}$ and $s_{i,k,t}^{G}$.

$$R_{i,t}^{G\max} = \sum_{k=1}^{n_k} \left(R_{i,k}^{GD\max} \cdot z_{i,k,t}^{G} + \varphi_{i,k}^{G} \cdot s_{i,k,t}^{G} \right) \tag{27}$$

Constraints Eqs (21)–(22) and Eqs (25)–(27) constitute the linearized ramping-frequency regulation unified constraint model for thermal units. Compared with the original nonlinear model Eqs (19)–(20), this linearized formulation is more amenable to solution using conventional mixed-integer linear programming (MILP) methods.

4. Optimal scheduling model for coordinated ramping-frequency regulation of ESSs and thermal units

In this section, we integrate the developed models of ESSs and thermal units to establish an overall optimal scheduling framework, enabling the coordinated participation of ESSs and thermal units in combined ramping-frequency regulation services.

4.1. Optimization objective

The objective of the optimization is to minimize the total system cost, expressed mathematically as:

$$\min \quad C_{Energy} + C_{Ramp} + C_{Regulation} \tag{28}$$

where C_{Energy}, C_{Ramp}, and $C_{Regulation}$ represent the energy cost, ramping cost, and frequency regulation cost, respectively. These components are further defined as:

$$C_{Energy} = \sum_{t=1}^{N_T}\sum_{i=1}^{N_G}\left(a_i^G + b_i^G \cdot P_{i,t}^G + c_i^G \cdot \left(P_{i,t}^G\right)^2 + c_i^{SU} \cdot x_{i,t} + c_i^{SD} \cdot y_{i,t}\right) + \sum_{t=1}^{N_T}\sum_{w=1}^{N_W} p_{WC} \cdot P_{w,t}^{WC} \tag{29}$$

$$C_{Ramp} = \sum_{t=1}^{N_T}\sum_{i=1}^{N_G} p_{RAG} \cdot \left(R_{i,t}^{G\uparrow} + R_{i,t}^{G\downarrow}\right) + \sum_{t=1}^{N_T}\sum_{e=1}^{N_E} p_{RAE} \cdot \left(R_{e,t}^{E\uparrow} + R_{e,t}^{E\downarrow}\right) \tag{30}$$

$$C_{Regulation} = \sum_{t=1}^{N_T}\sum_{i=1}^{N_G} p_{RFG} \cdot r_{i,t}^{G} + \sum_{t=1}^{N_T}\sum_{e=1}^{N_E} p_{RFE} \cdot r_{e,t}^{E} \tag{31}$$

where N_G denotes the number of generators, N_W denotes the number of wind farms, N_E denotes the number of ESSs, N_T denotes the number of time intervals, c_i^{SU} and c_i^{SD} represent start-up and shut-down costs, $P_{w,t}^{WC}$ is the wind curtailment power of wind farm w at time t, and p_{WC} is the penalty price for wind curtailment. p_{RAG}, p_{RAE}, p_{RFG}, and p_{RFE} represent the unit prices for ramping and frequency regulation services provided by thermal units and ESSs, respectively. The energy cost C_{Energy} covers thermal generation, start-up/shutdown, and wind curtailment costs, while C_{Ramp} and $C_{Regulation}$ reflect the expenses of providing ramping and frequency regulation ancillary services by both thermal units and ESSs.

It is worth noting that the proposed model is formulated as a single-objective economic dispatch rather than a multi-objective optimization. Therefore, the price parameters (p_{RAG}, p_{RAE}, p_{RFG}, and p_{RFE}) are explicit market clearing prices instead of subjective weighting coefficients. Driven by this unified economic objective, the system automatically achieves an optimal trade-off mechanism: While ESSs can reduce the system's ancillary service costs by providing ramping and regulation, their frequent charge/discharge actions inevitably incur implicit physical energy losses due to charging and discharging efficiencies (η_{ch} and η_{disch}), which in turn increases the energy cost C_{Energy}. Thus, the objective function inherently captures this coupled economic-physical trade-off.

4.2. Constraints

(1) Power balance constraint

The active power balance constraint can be expressed as:

$$\sum_{i=1}^{N_G} P_{i,t}^{G} + \sum_{w=1}^{N_W} (P_{w,t}^{W*} - P_{w,t}^{WC}) + \sum_{e=1}^{N_E} P_{e,t}^{E} = \sum_{d=1}^{N_D} P_{d,t}^{D*} \tag{32}$$

where $P_{w,t}^{W*}$ and $P_{d,t}^{D*}$ denote the forecasted wind power and load, respectively, and N_D represents the number of load buses.

(2) Branch power flow constraint

The power flow on branch l at time t can be described as:

$$P_{l,t}^{L} = \sum_{i=1}^{N_G} Q_{l,i}^{G} \cdot P_{i,t}^{G} + \sum_{w=1}^{N_W} Q_{l,w}^{W} \cdot (P_{w,t}^{W*} - P_{w,t}^{WC}) + \sum_{e=1}^{N_E} Q_{l,e}^{E} \cdot P_{e,t}^{E} + \sum_{d=1}^{N_D} Q_{l,d}^{D} \cdot (-P_{d,t}^{D*}) \tag{33}$$

where $Q_{l,i}^{G}$, $Q_{l,w}^{W}$, $Q_{l,e}^{E}$, and $Q_{l,d}^{D}$ are the corresponding coefficients in the sensitivity matrices of generators, wind farms, ESSs, and loads, respectively.

To map these sensitivity coefficients to the network topology, let $b_{\mathrm{G}}(i)$, $b_{\mathrm{W}}(\mathrm{w})$, $b_{\mathrm{E}}(e)$, and $b_{\mathrm{D}}(d)$ denote the mapping functions that return the corresponding bus index k to which the i-th generator, w-th wind farm, e-th ESS, and d-th load are connected. Under the DC power flow assumption, these sensitivity coefficients are computed from the network susceptance matrix **B** as follows:

$$\begin{cases} Q_{l,i}^{G} = \dfrac{1}{x_l}\left([\mathbf{B}^{-1}]_{m,b_G(i)} - [\mathbf{B}^{-1}]_{n,b_G(i)}\right) \\ Q_{l,w}^{W} = \dfrac{1}{x_l}\left([\mathbf{B}^{-1}]_{m,b_W(w)} - [\mathbf{B}^{-1}]_{n,b_W(w)}\right) \\ Q_{l,e}^{E} = \dfrac{1}{x_l}\left([\mathbf{B}^{-1}]_{m,b_E(e)} - [\mathbf{B}^{-1}]_{n,b_E(e)}\right) \\ Q_{l,d}^{D} = \dfrac{1}{x_l}\left([\mathbf{B}^{-1}]_{m,b_D(d)} - [\mathbf{B}^{-1}]_{n,b_D(d)}\right) \end{cases}$$

where x_l is the reactance of branch l, and m, n are its terminal buses.

Considering the uncertainties of wind generation and load demand, the branch power flow constraint can be formulated as a chance constraint:

$$\Pr\{P_{l,t}^{L} < P_{l}^{L\max}\} \geq \eta_l \tag{34}$$

where P_{l}^{Lmax} is the maximum permissible power flow on branch l, and η_l denotes the confidence level at which the constraint is satisfied. Assuming that the forecast errors of wind power ($P_{w,t}^{W*}$) and load ($P_{d,t}^{D*}$) follow a normal distribution, substituting Eq (33) into (34) and simplifying yields:

$$P_l^{L\max} - \sum_{i=1}^{N_G} Q_{l,i}^G \cdot P_{i,t}^G + \sum_{w=1}^{N_W} Q_{l,w}^W \cdot P_{w,t}^{WC} - \sum_{e=1}^{N_E} Q_{l,e}^E \cdot P_{e,t}^E - \sum_{w=1}^{N_W} Q_{l,w}^W \cdot P_{w,t}^{W*} + \sum_{d=1}^{N_D} Q_{l,d}^D \cdot P_{d,t}^{D*} \geq \Phi^{-1}(\eta_l) \cdot \sqrt{\sum_{w=1}^{N_W} (Q_{l,w}^W)^2 \cdot \delta_{w,t}^2 + \sum_{d=1}^{N_D} (Q_{l,d}^D)^2 \cdot \delta_{d,t}^2} \tag{35}$$

where Φ^{-1} denotes the inverse cumulative distribution function of the standard normal distribution, and $\delta_{w,t}$, $\delta_{d,t}$ are the standard deviations of the wind power and load forecast errors, respectively.

(3) Frequency regulation reserve constraint

Similar to Eq (35), considering the uncertainties of wind generation and load forecasting, the frequency regulation (FR) reserve constraint can be expressed as:

$$\sum_{i=1}^{N_G} r_{i,t}^G + \sum_{e=1}^{N_E} r_{e,t}^E \geq \Phi^{-1}(\eta) \cdot \sqrt{\sum_{d=1}^{N_D} \delta_{d,t}^2 + \sum_{w=1}^{N_W} \delta_{w,t}^2} \tag{36}$$

where η denotes the confidence level ensuring that the frequency regulation reserve requirement is satisfied.

(4) Energy storage constraints

The constraints for the ESS are adopted from Section 2, including constraints Eqs (1)–(4), (6)–(7), and (15).

(5) Thermal unit constraints

The constraints for thermal generating units are adopted from Section 3, including constraints Eqs (16)–(18), (21)–(22), and (25)–(27).

As can be seen from the above formulations, all objective functions and constraints are linear except for the quadratic term in the objective function Eq (29). This indicates that the proposed CCP can be effectively solved using a MIQP algorithm with strict convergence guarantees. Furthermore, the computational complexity of the CCP method is consistent with that of the deterministic model, which is significantly lower than that of Stochastic Programming (SP) or Robust Optimization (RO) algorithms.

5. Case study

In this section, we verify the effectiveness of the proposed method through case studies. The analysis is conducted based on the IEEE 6-bus system, which consists of six buses and seven transmission lines, with generators at buses 1, 2, and 6, as shown in Figure 2. To investigate the coordinated optimization of ESSs and generators under uncertain renewable energy conditions, a wind farm is integrated at bus 1, while ESSs are installed at buses 4 and 5. The case studies are performed on a computer with an Intel(R) Core(TM) i5-1035G1 CPU @ 1.00GHz (1.19 GHz).

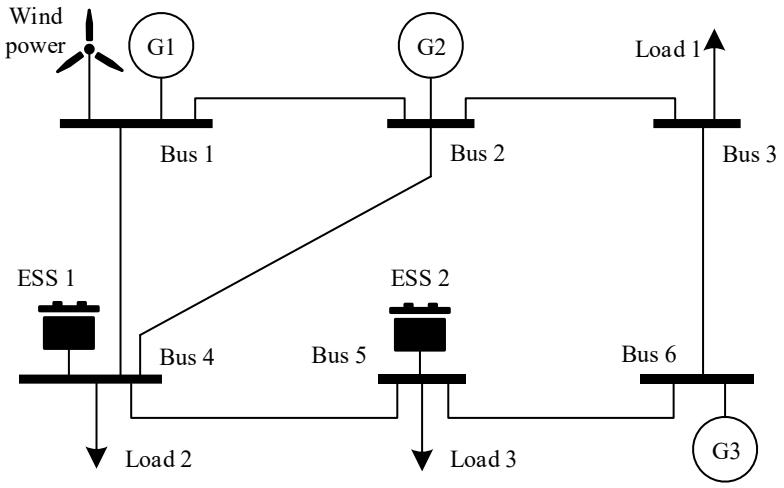

Figure 2. IEEE 6-bus system integrated with wind power and ESSs.

5.1. Comparison of optimization results with different PWL segment numbers

In this subsection, we discuss the optimization results of thermal units with nonlinear ramping characteristics under different numbers of PWL segments. By balancing computational efficiency and modeling accuracy, an appropriate PWL segmentation level is determined. To analyze the impact of different PWL segment numbers on the optimization outcomes, the following three models are considered:

(1) Linear model: The PWL segment number is set to 1, and the nonlinear ramping characteristics are ignored.

(2) PWL model (2 segments): The ramping curve is approximated using two linear segments.

(3) PWL model (4 segments): The ramping curve is approximated using four linear segments.

The ramping characteristics of the three thermal units under different models are shown in Figure 3, where the Nonlinear model represents the original nonlinear ramping characteristics of the units, which must be linearized using the above three models for optimization. As shown in Figure 3, the linear model (with one PWL segment) exhibits a large deviation from the original nonlinear model. As the number of PWL segments increases, the PWL model becomes progressively closer to the nonlinear model. When the number of segments reaches four, the deviation between the PWL model and the original nonlinear ramping characteristics becomes negligible.

To further analyze the optimization results under different ramping characteristic models, Figure 4 presents the optimization outcomes for the Linear model (equivalent to one PWL segment) and the PWL models with 2 and 4 segments. As shown in the scheduling results (first row of Figure 4), noticeable differences can be observed in the optimal dispatch of generators and ESSs under different segmentation schemes, particularly during generator ramping periods. Moreover, as indicated by the computation time and integrated power error of the thermal units across the three models, the integrated power error decreases significantly as the number of PWL segments increases, while the computation time rises sharply. When the PWL segment number reaches 4, the optimization solving time approaches 100 s, posing challenges for real-time scheduling applications. In contrast, the 2-segment PWL model completes the optimization within 40 s despite the modest hardware configuration. To balance model accuracy and computational efficiency, the PWL model with 2 segments is adopted in the subsequent case studies.

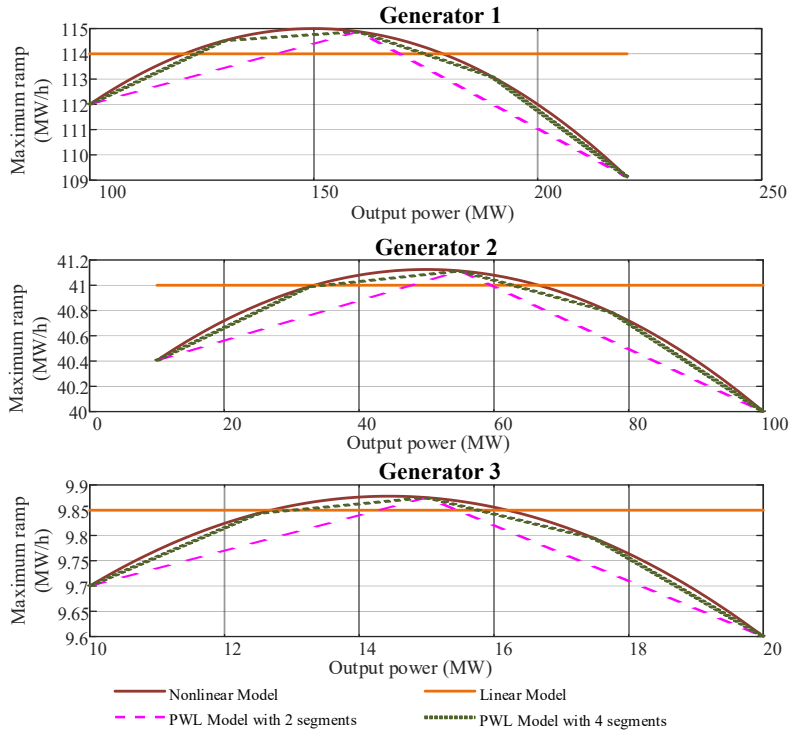

Figure 3. Nonlinear ramping characteristics of thermal generating units and their PWL approximations under different segmentation methods.

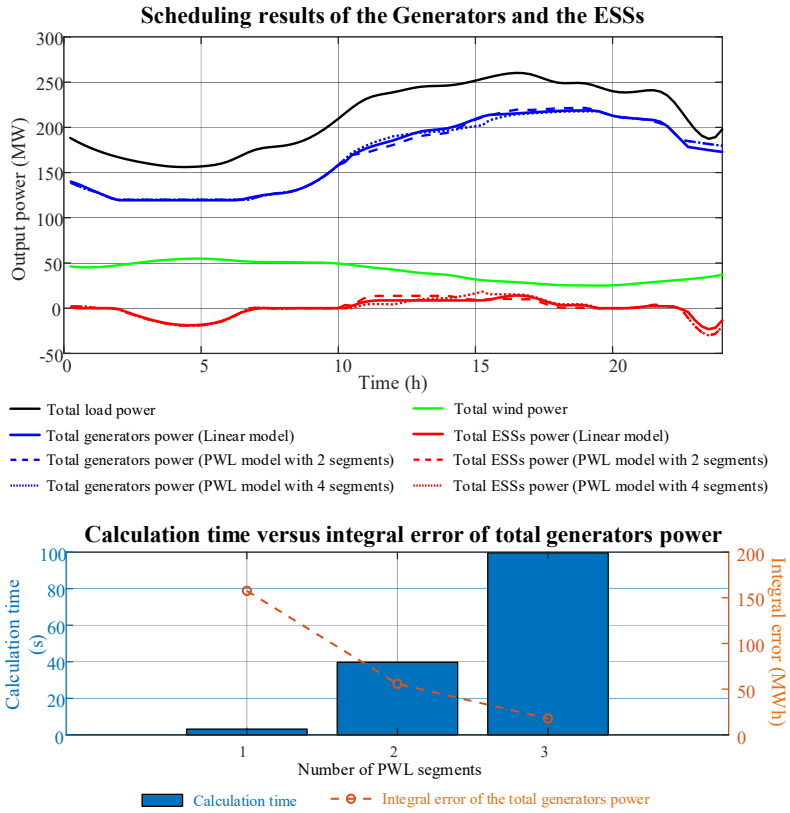

Figure 4. Comparison of optimization results for thermal generating units under different PWL segmentation methods.

It should be noted that although the 2-segment PWL inevitably introduces slight capacity fitting errors, these are handled safely through a conservative under-approximation strategy. By explicitly setting the PWL segments slightly below the actual nonlinear physical curve, the solver is prevented from overestimating the total available ramping capability. Consequently, the co-optimized capacities allocated for ramping and frequency regulation will never exceed the true physical headroom of the units, rigorously guaranteeing the physical feasibility of the scheduling results during real-time execution.

Figure 5 illustrates the optimal scheduling results of system resources when the number of PWL segments is set to two, including the output power of each generator, the charging/discharging power, and the SOC of the ESSs. As shown in Figure 5, the ESSs charge during the low-load period (2:00–5:00) to perform valley filling and discharge during the peak-load period (15:00–18:00) to achieve peak shaving. In addition, during the load-ramping period (10:00–15:00), the ESSs provide ramping support, effectively reducing the system's dependence on generator ramping, mitigating the rate of change in generator power, and thereby enhancing system reliability and operational efficiency.

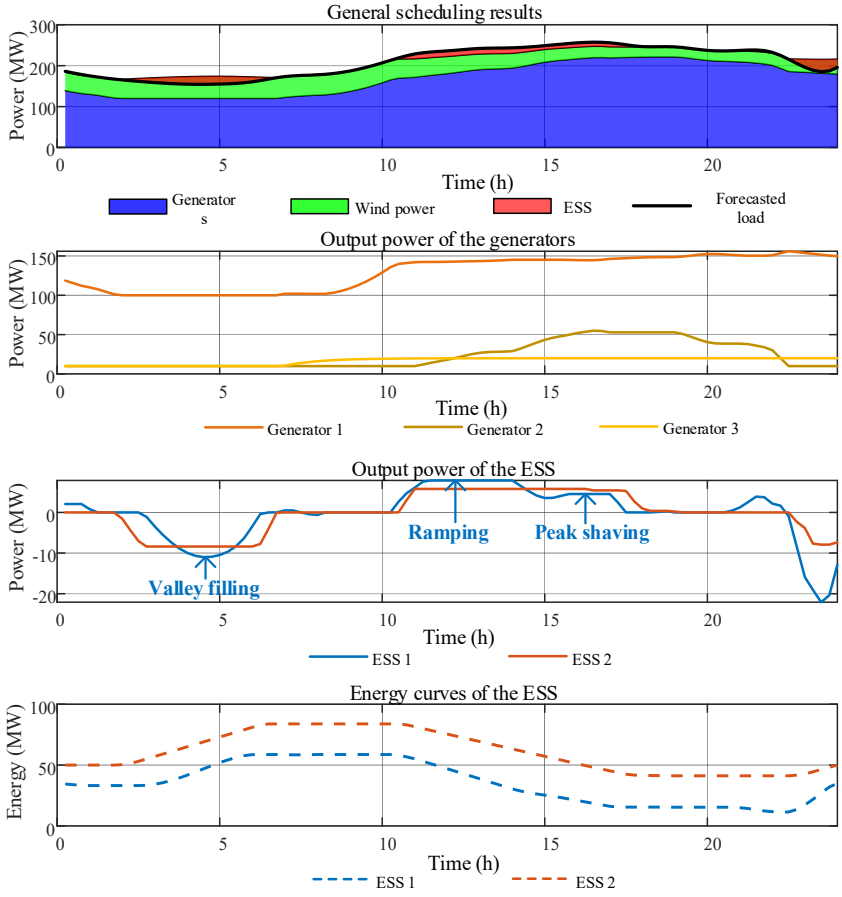

Figure 5. Optimal scheduling results under the PWL model with two segments.

5.2. Validation of the unified constraint model

In this subsection, the effectiveness of the proposed unified ramp-frequency regulation constraint model is verified through comparative analysis. To this end, the following two models are considered:

(1) Model with non-unified constraints: In this model, the unified ramp-frequency regulation constraints given by Eqs (6)–(7) and (21)–(22) are not applied. Instead, $R^{E}_{e,t}$ and $r^{E}_{e,t}$, as well as $R^{G}_{i,t}$

and $r_{i,t}^{G}$, are constrained independently by their respective upper and lower limits.

(2) Model with unified constraints: This model adopts the proposed unified ramp-frequency regulation constraints as formulated in Eqs (6)–(7) and (21)–(22), enabling coordinated sharing of ramping and frequency regulation capacities between generators and ESSs.

The optimal scheduling results of generators and ESSs under the two models are shown in Figure 6, and the allocation of ramping power and frequency regulation reserves between generators and ESSs under both scenarios is illustrated in Figure 7. To further quantify the performance improvement, the key operational metrics are summarized in Table 1.

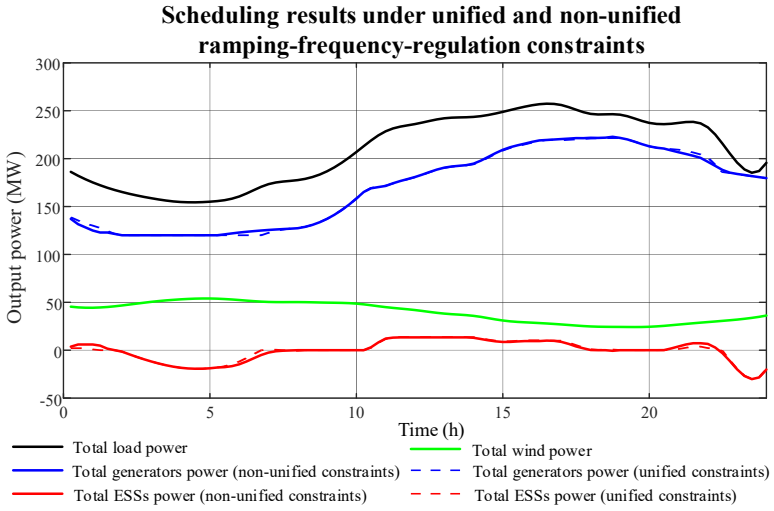

Figure 6. Optimal scheduling results of generators and ESSs under unified and non-unified ramp-frequency regulation constraints.

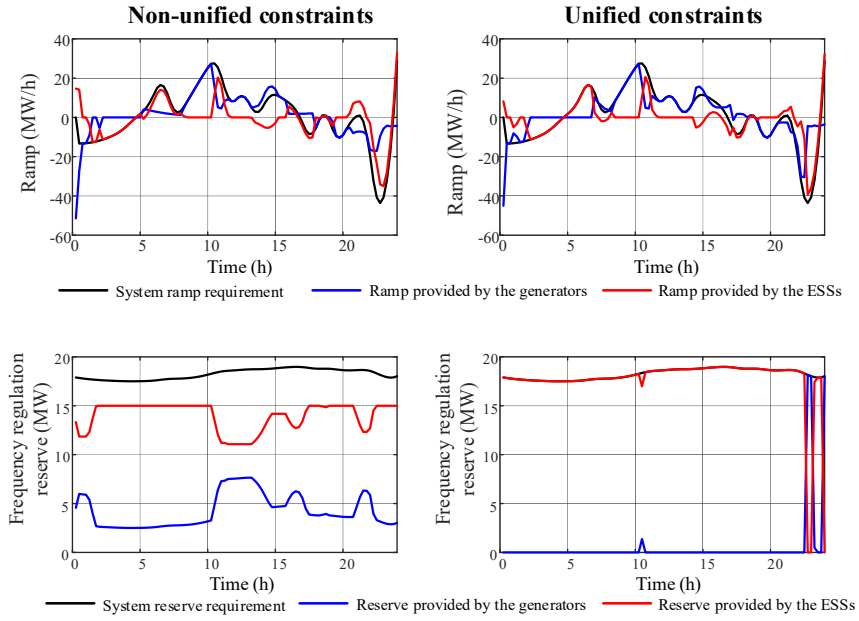

Figure 7. Allocation of ramping power and frequency regulation reserves between generators and ESSs under unified and non-unified ramp-frequency regulation constraints.

Table 1. Quantitative comparison between unified and non-unified constraint models.

	Non-Unified Constraints	Unified Constraints	Improvement Percent
ESS FR Capacity (MWh)	335.78	423.84	26.227%
Ramping Cost C_{Ramp} (\$)	505.47	498.56	−1.3671%
Frequency Regulation Cost $C_{Regulation}$ (\$)	529.51	525.99	−0.66526%

As observed from Figure 6, there exist only minor differences in the optimal scheduling results between the unified and non-unified constraint models. Since the unified ramp-frequency regulation constraint primarily affects the participation of generators and ESSs in ramping and reserve provision, the discrepancies between the two models mostly occur during the ramp-up and ramp-down periods.

From Figure 7 and Table 1, it can be seen that, under the non-unified constraint model, the ramping power and frequency regulation reserves cannot be shared, requiring generators and ESSs to independently provide certain amounts of regulation reserves. In contrast, under the unified constraint model, most of the frequency regulation reserve is undertaken by ESSs, while generators provide reserves only during the periods when ESSs are engaged in ramping. This is because, in the unified constraint model, ramping power and frequency regulation reserves can be jointly allocated, enabling ESSs to obtain a greater share of frequency regulation. As shown in Table 1, the ESS FR capacity increases by 26.227% under the unified model, which confirms its effectiveness in alleviating capacity redundancy caused by independent service requirements.

5.3. Adaptability and robustness analysis under multiple scenarios

To comprehensively evaluate the adaptability and robustness of the proposed strategy under various operating conditions, in this subsection, we compare the optimization results under varying confidence levels of frequency regulation reserves, line flow limits, and energy capacity constraints. By adjusting these confidence levels, the model effectively simulates different scenarios, including renewable energy penetration rates, load disturbance patterns, and energy storage capacity uncertainty levels.

The confidence levels of frequency regulation reserves (η) and line flow limits (η_l), defined in constraints Eqs (35) and (36), respectively, reflect the system's tolerance to wind power and load uncertainties. Moreover, the energy capacity confidence level (η_e), defined in constraint Eq (15), represents the tolerance to energy storage capacity uncertainty. To analyze the system's adaptability under different renewable penetration and load disturbance patterns, three scenarios are considered for frequency regulation and line flow constraints: Low confidence: (η = 0.95, η_l = 0.96), Medium confidence: (η = 0.98, η_l = 0.99), and High confidence: (η = 0.99, η_l = 0.995). The corresponding optimization results are shown in Figure 8 with the statistic results listed in Table 2. Similarly, to evaluate the robustness against ESS capacity uncertainty, three confidence levels are considered for the energy capacity constraint: Low confidence (η_e = 0.95), Medium confidence (η_e = 0.98), and High confidence (η_e = 0.99). The corresponding optimization results are shown in Figure 9 with the statistic results listed in Table 3.

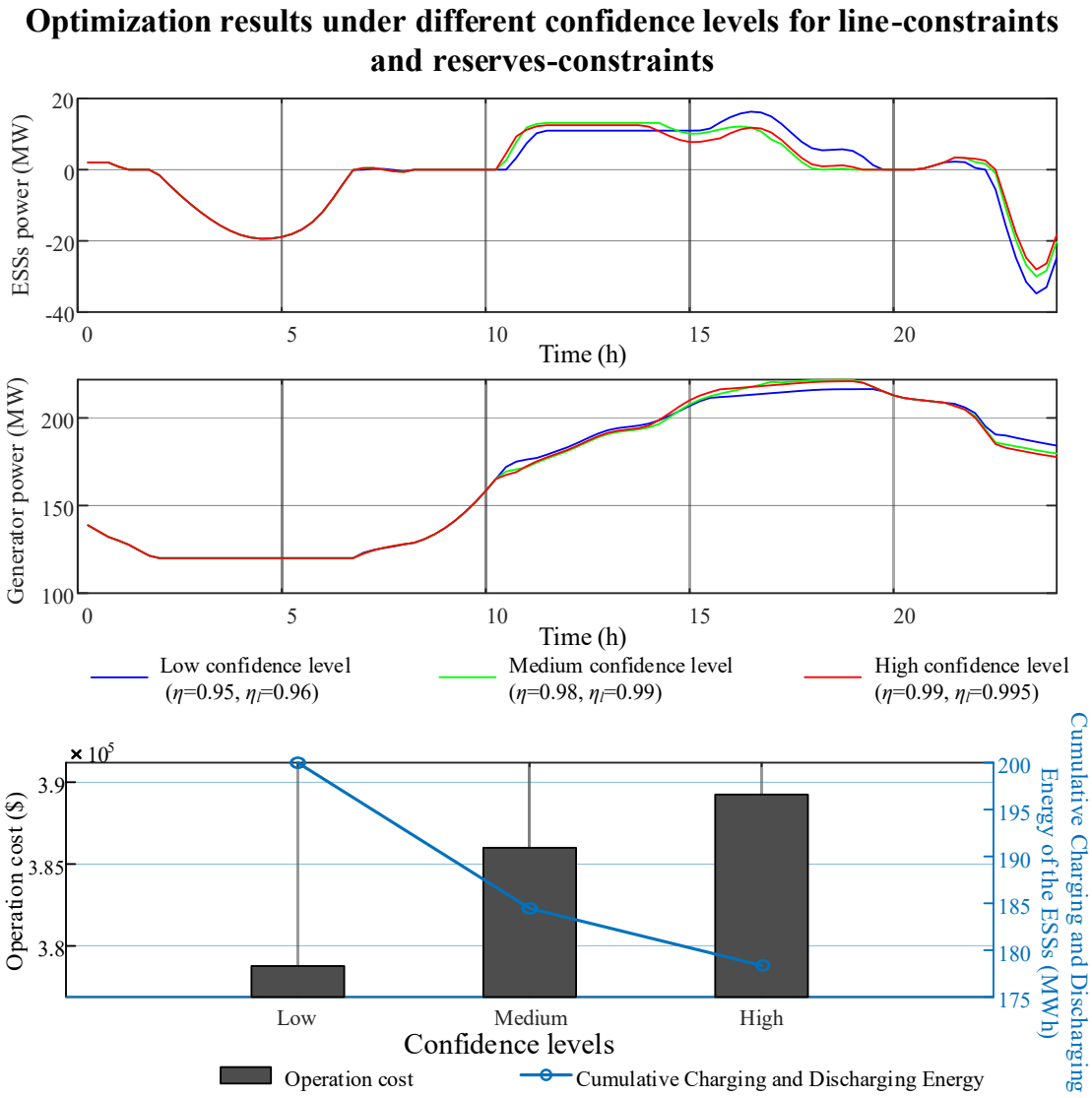

Figure 8. Optimization results under different confidence levels for line-constraints and reserve-constraints. First row: Total ESS power under different confidence levels. Second row: Total generator power under different confidence levels. Third row: Operating cost and cumulative charging/discharging power of ESSs.

Table 2. Optimization results under different confidence levels for line-constraints and reserves-constraints.

Confidence levels	Cumulative charging and discharging energy of the ESSs (MWh)	Operation cost ($)
Low (η = 0.95, η_l = 0.96)	200.35	3.784×10^5
Medium (η = 0.98, η_l = 0.99)	184.45	3.862×10^5
High (η = 0.99, η_l = 0.995)	178.31	3.891×10^5

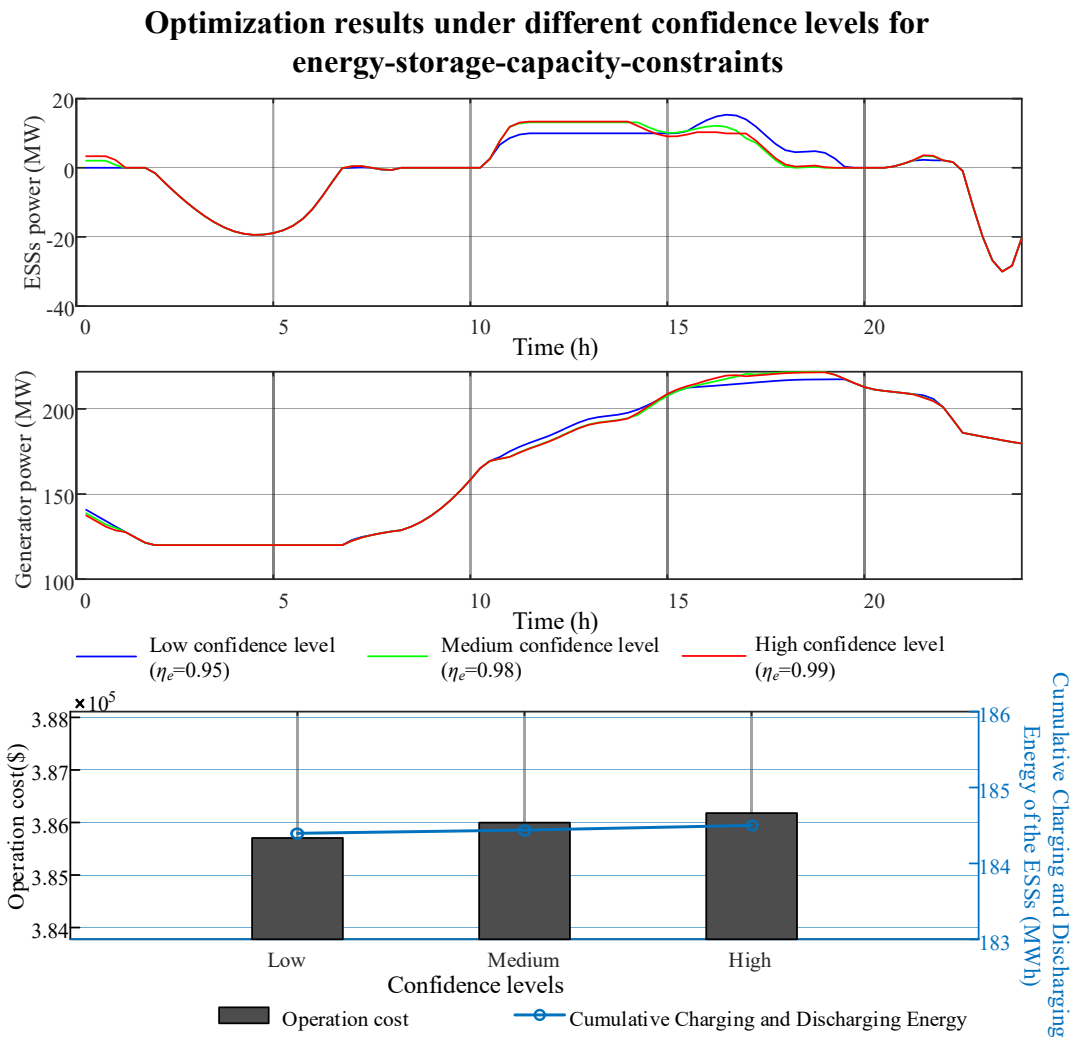

Figure 9. Optimization results under different confidence levels for energy-storage-capacity-constraints. First row: Total ESS power under different confidence levels. Second row: Total generator power under different confidence levels. Third row: Operating cost and cumulative charging/discharging power of ESSs.

Table 3. Optimization results under different confidence levels for energy-storage-capacity-constraints.

Confidence levels	Cumulative Charging and Discharging Energy of the ESSs (MWh)	Operation cost ($)
Low (η_e = 0.95)	184.44	3.858×10^5
Medium (η_e = 0.98)	184.46	3.860×10^5
High (η_e = 0.99)	184.51	3.862×10^5

From Figure 8, it can be observed that when the confidence levels of frequency regulation and line flow constraints are relatively low, the ESSs contribute more to peak shaving and less to ramping support. In this case, the overall utilization of ESSs is higher, while the total operational cost is lower. Conversely, when the confidence levels are higher, the ESSs provide less peak shaving but more ramping support to reserve additional capacity for frequency regulation, resulting in reduced ESS utilization and increased operational cost.

From Figure 9, as the energy capacity confidence level increases from low to high, the ESSs gradually shift from providing more peak shaving to contributing more ramping support. Both the overall ESS utilization and system operational cost show a slight increase. The higher energy capacity confidence level limits the available usable energy of the ESSs, which increases system cost. However, since the proposed optimization framework adopts a unified ramp-frequency regulation constraint, part of the ESS capacity originally used for peak shaving and frequency regulation is automatically reallocated to ramping, resulting in only minor variations in overall ESS utilization and system operating cost.

6. Conclusions

In this paper, we propose an optimal scheduling strategy for power systems considering energy storage capacity uncertainty and unified ramping-frequency regulation constraints. Specifically, ramping-FR unified constraint models are established for ESSs and thermal units. To address the uncertainty of storage capacity, a chance-constrained model based on probabilistic confidence levels is developed, while a PWL model is formulated to capture the nonlinear ramping characteristics of thermal units. An integrated optimization model of ESSs and thermal units is then constructed and solved using MIQP. The case study analysis leads to the following conclusions:

1) Compared with non-unified constraint models, the proposed ramping-frequency regulation unified constraint model enables the sharing of ESS ramping power and frequency regulation reserves within a single constraint framework. Consequently, ESSs can provide larger frequency regulation reserves while participating in ramping, thereby improving overall optimization efficiency.

2) Compared with a conventional linear model, the proposed PWL model for thermal units more accurately represents their intrinsic nonlinear ramping characteristics. Increasing the number of PWL segments reduces the model's cumulative error, but also significantly increases computational time.

3) The choice of the probabilistic confidence level has a substantial impact on the optimization results. As the confidence level of the storage capacity constraint increases, ESSs shift from primarily performing peak shaving to undertaking more ramping tasks, which leads to a corresponding increase in overall operating costs.

Despite the demonstrated effectiveness, this study has the following limitations:

1) Computational Scalability: The PWL approximation introduces a substantial number of binary variables. Given the NP-hard nature of MIQP, the computational burden scales exponentially, posing challenges for large-scale systems (e.g., IEEE 118-bus systems).

2) Uncertainty Distribution under Extreme Scenarios: To ensure mathematical tractability, the ESS capacity uncertainty is modeled using a normal distribution. However, under extreme operating scenarios, the actual State of Charge (SOC) may exhibit non-Gaussian characteristics due to strict physical boundaries (e.g., a Beta distribution bounded between 0 and 1).

To address the above issues, in future work, we will focus on a selective PWL framework, applying PWL only to units with severe nonlinearities, to strictly balance accuracy and efficiency. In addition, more general probability distributions will be integrated into the chance-constrained framework to enhance the model's adaptability to extreme conditions.

Use of AI tools declaration

The authors declare they have not used Artificial Intelligence (AI) tools in the creation of this article.

Acknowledgments

This work is supported by State Grid Jiangsu Electric Power Co., Ltd. Electric Power Science Research Institute under the Project "Research on the participation mechanism of ramp-up and frequency regulation services considering the confidence level of new energy storage capacity" (Project No. J2025023).

Conflicts of interest

The authors declare that there is no conflicts of interest regarding the publication of this paper.

Author contributions

The authors confirm contribution to the paper as follows: Haiyun An: Conceptualization, methodology, formal analysis, writing—original draft; Tianhui Zhao: supervision, resources, project administration; Yuqing Bao: writing—review and editing, project administration, validation; Jingbo Zhao: writing—review and editing, project administration, validation. All authors have read and agreed to the published version of the manuscript.

Reference

1. Yu Y, Jiang H, Zhang N, et al. (2025) Revisiting capacity value of variable renewable energy generation in power systems with high renewable energy penetration. *J Mod Power Syst Clean Energy* 13: 1593–1603. https://doi.org/10.35833/MPCE.2024.001101
2. Bao YQ, Song XR, Zhou PC (2025) Stackelberg-game-based energy optimization strategy for interactive energy use of flexible manufacturing industrial parks. *Appl Energy* 401: 126701. https://doi.org/10.1016/j.apenergy.2025.126701
3. Correa-Posada CM, Morales-España G, Dueñas P, et al. (2017) Dynamic ramping model including intraperiod ramp-rate changes in unit commitment. *IEEE Trans Sustainable Energy* 8: 43–50. https://doi.org/10.1109/TSTE.2016.2578302
4. Gong Y, Jiang Q, Baldick R (2016) Ramp event forecast based wind power ramp control with energy storage system. *IEEE Trans Power Syst* 31: 1831–1844. https://doi.org/10.1109/TPWRS.2015.2445382
5. Bao YQ, Yu QQ, Chen Y, et al. (2024) Wind power smoothing control by energy storage based on area-equilibrium empirical mode decomposition. *J Mod Power Syst Clean Energy* 13: 1238–1247. https://doi.org/10.35833/MPCE.2024.000674
6. Zhang M, Xiao Y, Gao Y, et al. (2024) An novel soft-linking model: Coordinating the regulative flexibility and operational stability of pumped storage units. *Appl Energy* 374: 123942. https://doi.org/10.1016/j.apenergy.2024.123942

7. Rajamand S (2021) Load frequency control and dynamic response improvement using energy storage and modeling of uncertainty in renewable distributed generators. *J Energy Storage* 37: 102467. https://doi.org/10.1016/j.est.2021.102467
8. Pan X, Xu H, Lu C, et al. (2016) Energy storage system control strategy in frequency regulation. *2016 IEEE International Conference on Automation Science and Engineering (CASE)*, 664–669. https://doi.org/10.1109/COASE.2016.7743466
9. Xu C, Zhao D, Feng X, et al. (2025) Multi-damping frequency-constrained unit commitment and multi-reserve resource allocation for RES-penetrated power systems. *CSEE J Power Energy Syst* 1–14. https://doi.org/10.17775/CSEEJPES.2024.02590
10. Shi Y, Xu B, Wang D, et al. (2018) Using battery storage for peak shaving and frequency regulation: Joint optimization for superlinear gains. *IEEE Trans Power Syst* 33: 2882–2894. https://doi.org/10.1109/TPWRS.2017.2749512
11. Jo J, Park J (2020) Demand-Side management with shared energy storage system in smart grid. *IEEE Trans Smart Grid* 11: 4466–4476. https://doi.org/10.1109/TSG.2020.2980318
12. Nazemi M, Dehghanian P, Lu X , et al. (2021) Uncertainty-Aware deployment of mobile energy storage systems for distribution grid resilience. *IEEE Trans Smart Grid* 12: 3900–3912. https://doi.org/10.1109/TSG.2021.3064312
13. Li J, Zhang M, Shuai Z, et al. (2025) Two-Stage hybrid optimization of aggregated distributed generalized energy storages for complete uncertainty elimination. *IEEE Trans Smart Grid* 16: 2075–2086. https://doi.org/10.1109/TSG.2024.3525070
14. Cheng J, Chu F, Zhou M (2018) An improved model for parallel machine scheduling under time-of-use electricity price. *IEEE Trans Automat Sci Eng* 15: 896–899. https://doi.org/10.1109/TASE.2016.2631491
15. Liu Y, Zeng W, Chen M, et al. (2024) Chance-constrained scheduling considering frequency support from electric vehicles under multiple uncertainties. *IET Renewable Power Gener* 18: 4348–4359. https://doi.org/10.1049/rpg2.13171
16. Qiu Z, Zhang W, Lu S, et al. (2022) Charging-rate-based battery energy storage system in wind farm and battery storage cooperation bidding problem. *CSEE J Power Energy Syst* 8: 659–668. https://doi.org/10.17775/CSEEJPES.2021.00230
17. Kim HJ, Sioshansi R, Lannoye E, et al. (2025) Assessing the capacity value of energy storage that provides frequency regulation. *IEEE Trans Power Syst* 40: 2661–2673. https://doi.org/10.1109/TPWRS.2024.3501095
18. Zhang S, Mishra Y, Ledwich G, et al. (2013) The operating schedule for battery energy storage companies in electricity market. *J Mod Power Syst Clean Energy* 1: 271–280. https://doi.org/10.1007/s40565-013-0039-6
19. Goh HH, Ou Y, Dai W, et al. (2025) Frequency-constrained unit commitment considering coordinated frequency control strategy of wind turbines and energy storage system. *J Mod Power Syst Clean Energy* 13: 1933–1944. https://doi.org/10.35833/MPCE.2024.000976
20. Chen Y, Quan H, Xiao J, et al. (2025) Frequency stability-constrained optimal scheduling with energy storage support for microgrid under uncertainty. *2025 10th Asia Conference on Power and Electrical Engineering (ACPEE)*, 2411–2416. https://doi.org/10.1109/ACPEE64358.2025.11041225

21. He G, Chen Q, Kang C, et al. (2017) Cooperation of wind power and battery storage to provide frequency regulation in power markets. *IEEE Trans Power Syst* 32: 3559–3568. https://doi.org/10.1109/TPWRS.2016.2644642
22. Wen Y, Li W, Huang G, et al. (2016) Frequency dynamics constrained unit commitment with battery energy storage. *IEEE Trans Power Syst* 31: 5115–5125. https://doi.org/10.1109/TPWRS.2016.2521882
23. Martin S, Onori S, Rajagopal R (2022) Effect of state of charge uncertainty on battery energy storage systems. *IFAC-PapersOnLine* 55: 740–745. https://doi.org/10.1016/j.ifacol.2022.11.270
24. Rosewater D, Ferreira S, Schoenwald D, et al. (2019) Battery energy storage state-of-charge forecasting: Models, optimization, and accuracy. *IEEE Trans Smart Grid* 10: 2453–2462. https://doi.org/10.1109/TSG.2018.2798165
25. Peng S, Chen C, Shi H, et al. (2017) State of charge estimation of battery energy storage systems based on adaptive unscented kalman filter with a noise statistics estimator. *IEEE Access* 5: 13202–13212. https://doi.org/10.1109/ACCESS.2017.2725301

AIMS Press